





## Investigation of the difference in charge radii of mirror pairs with deep Bayesian neural networks

X. Zhang (张鑫) <sup>1</sup>, H. He (何红斌)<sup>2</sup>, G. Qu (曲国峰)<sup>1</sup>, X. Liu (刘星泉) <sup>1,\*</sup>, H. Zheng (郑华) <sup>2,†</sup>,  
W. Lin (林炜平)<sup>1</sup>, J. Han (韩纪锋)<sup>1</sup>, P. Ren (任培培)<sup>1</sup> and R. Wada <sup>3</sup>

<sup>1</sup>Key Laboratory of Radiation Physics and Technology of the Ministry of Education, *Sichuan University*, Chengdu 610064, China

<sup>2</sup>School of Physics and Information Technology, *Shaanxi Normal University*, Xi'an 710119, China

<sup>3</sup>Cyclotron Institute, *Texas A&M University*, College Station, Texas 77843, USA



(Received 10 January 2024; revised 27 March 2024; accepted 14 June 2024; published 12 July 2024)

The relationship of the root-mean-square (rms) charge radius difference  $\Delta R_{\text{ch}}^{\text{mir}}$  of mirror pairs and the isospin asymmetry  $(N - Z)/A$  is investigated using a newly developed deep Bayesian neural network (DBNN) approach. The DBNN approach with optimized architecture and input features demonstrates superior predictive capability for nuclear rms charge radii  $R_{\text{ch}}$  compared to previous machine learning approaches employing single-layer neural networks. Utilizing the DBNN-predicted  $R_{\text{ch}}$  values, a significant mass dependence of the  $\Delta R_{\text{ch}}^{\text{mir}}$  versus  $(N - Z)/A$  linear relationship, previously unobserved in experimental  $\Delta R_{\text{ch}}^{\text{mir}}$  analyses, is revealed. The physical existence and origin of the mass-dependent linear relationship between  $\Delta R_{\text{ch}}^{\text{mir}}$  and  $(N - Z)/A$  is explored using the microscopic Sky3D model and the macroscopic droplet model. Both Sky3D model and droplet model calculations indicate the physical existence of a mass-dependent linear relationship between  $\Delta R_{\text{ch}}^{\text{mir}}$  and  $(N - Z)/A$  in nature. Within the droplet model framework, the mass dependence is found to be closely associated with the ratio of the volume and surface symmetry energy coefficients, suggesting that such a mass-dependent  $\Delta R_{\text{ch}}^{\text{mir}}$  versus  $(N - Z)/A$  linear relationship could potentially serve as a probe for studying the surface component in nuclear symmetry energy in future.

DOI: [10.1103/PhysRevC.110.014316](https://doi.org/10.1103/PhysRevC.110.014316)

## I. INTRODUCTION

The overarching goal of nuclear physics is to unravel the fundamental properties of nuclei from their building blocks, protons and neutrons, and ultimately to determine the emergent complexity in the realm of the strong interaction. As one of the most fundamental nuclear parameters, nuclear root-mean-square (rms) charge radius  $R_{\text{ch}}$  characterizes the spatial charge arrangement in the atomic nucleus, and provides crucial information on nuclear deformation, shape coexistence, proton-neutron pairing correlations, etc. [1–5]. In particular, under the assumption of charge symmetry, the  $R_{\text{ch}}$  difference between a given mirror pair with interchanged numbers of protons and neutrons  $Z$  and  $N$  ( $Z > N$  and the same hereinafter),  $\Delta R_{\text{ch}}^{\text{mir}} \equiv R_{\text{ch}}(Z, X_N) - R_{\text{ch}}(N, Y_Z)$ , is a key observable that can be used as an isovector indicator of the nuclear equation of state [6–10]. Despite abundant information on the nuclear equation of state having been deduced from the limited amount of  $\Delta R_{\text{ch}}^{\text{mir}}$  data, revealing the basic properties of  $\Delta R_{\text{ch}}^{\text{mir}}$  across the nuclear chart and further developing a universal framework for their consistent description is a formidable challenge due to the lack of data, especially of mirror pairs far from the  $\beta$ -stability line [11,12].

To gain valuable insight into  $\Delta R_{\text{ch}}^{\text{mir}}$  in the unstable region, various approaches based on microscopic and macroscopic

theories have been developed to predict the  $R_{\text{ch}}$  values in the literature, i.e., density functional theory, the *ab initio* method, the droplet model for nuclear radii, etc. [13–16]. Great progress has been achieved in applying these approaches to systematically predict nuclear rms charge radii in a wide mass region in the past several decades. However, ambiguities still exist at present. For instance, the  $R_{\text{ch}}$  predictive performance strongly depends on the physical assumptions and the selection of effective interactions or energy density functional forms in models. Such ambiguities significantly impact further deduction of physical information from the predicted results. To address these issues, more efforts are therefore required. Recently, a surge of interest in applying machine learning approach for predicting the  $R_{\text{ch}}$  values has been observed [17–20]. In general, a neural network is able to acquire the fundamental correlation between the input feature representations and the target observable from the raw data via the training process, independently of any physical assumptions or effective interaction selections, so that applying machine learning technique for the  $R_{\text{ch}}$  prediction allows one to avoid the difficulties in theory arising from the quantum many-body problem, the complexity of nuclear force, etc.

Deep learning, being a novel branch of machine learning and significantly improving the state-of-the-art in various tasks such as image and speech recognition, natural language processing, and others [21], has recently inspired many applications in the field of nuclear physics [22–27]. Taking the advantage of deep learning in characterizing complex data sets, the goals of attaining more accurate  $R_{\text{ch}}$  prediction

\*Contact author: liuxingquan@scu.edu.cn

†Contact author: zhengh@snnu.edu.cn

across the nuclear chart and acquiring deeper understanding of  $\Delta R_{\text{ch}}^{\text{mir}}$  may be achieved. In 2023, Novario *et al.* found an interesting linear relationship between  $\Delta R_{\text{ch}}^{\text{mir}}$  and nuclear isospin asymmetry  $(N - Z)/A$  in the light and intermediate mass region using the coupled-cluster theory and the auxiliary field diffusion Monte Carlo method [9]. To provide deeper insights into the linear relationship of  $\Delta R_{\text{ch}}^{\text{mir}}$  and  $(N - Z)/A$  and acquire more valuable information on nuclear properties, more research is urgently required. In this article, we propose deep learning within the Bayesian framework [28] to predict the  $R_{\text{ch}}$  values to study the linear relationship of  $\Delta R_{\text{ch}}^{\text{mir}}$  and  $(N - Z)/A$  beyond the existing data. To ensure outstanding predictive performance for the present task, specific considerations are made in terms of selecting the input and the key hyperparameters related to the architecture in the deep Bayesian neural network (DBNN). We are going to show that the present DBNN has stronger predictive capability both in reproducing the existing data and in extrapolating the unmeasured data compared to any previous machine learning approaches with single-layer neural networks [17–20]. The linear relationship of  $\Delta R_{\text{ch}}^{\text{mir}}$  and  $(N - Z)/A$  is then studied using the DBNN-predicted  $R_{\text{ch}}$  values for the unmeasured nuclei. A detailed mass-dependent behavior of the  $\Delta R_{\text{ch}}^{\text{mir}}$  versus  $(N - Z)/A$  linear relationship is revealed in the mass  $A = 20$ –60 region in which only a limited amount of experimental  $\Delta R_{\text{ch}}^{\text{mir}}$  data are available, and its physical existence and origin are explored by comparing the results with those from the microscopic Sky3D model which solves time-dependent Hartree-Fock (TDHF) equation in a general three-dimensional geometry [29], and the macroscopic droplet model of Myers and Swiatecki [30]. Previous studies on nuclear symmetry energy have highlighted the conceptual necessity to incorporate a surface contribution to the symmetry energy [31,32]. However, the investigation of the surface component in the symmetry energy remains relatively lacking compared to the volume component, as is evident in the literature. In this work, the close correlation between the degree of the mass-dependent linear relationship predicted by DBNN and the surface component of the symmetry energy is further shown, and it will indicate a potential of the mass-dependent behavior as a promising probe for investigating the surface component in the symmetry energy.

## II. DESCRIPTION OF DBNN APPROACH

### A. Architecture

This work starts with describing the details that are critical to the DBNN approach and its implementation for the  $R_{\text{ch}}$  prediction. Figure 1 shows the general architecture of the DBNN proposed for predicting the  $R_{\text{ch}}$  values. As found in the figure, the DBNN can be treated as a nonlinear function  $F$  that maps  $I$  feature representations in the input layer  $\mathbf{X} = \{x_1, x_2, \dots, x_I\}$ , and a set of intrinsic parameters into a hierarchy of  $H$  layers of combinations with hidden neurons, and provides prediction for target observable  $t$  in the output layer. Following the standard practice [25,33–38], a feed-forward neural network model is used to transmit the input feature representations to

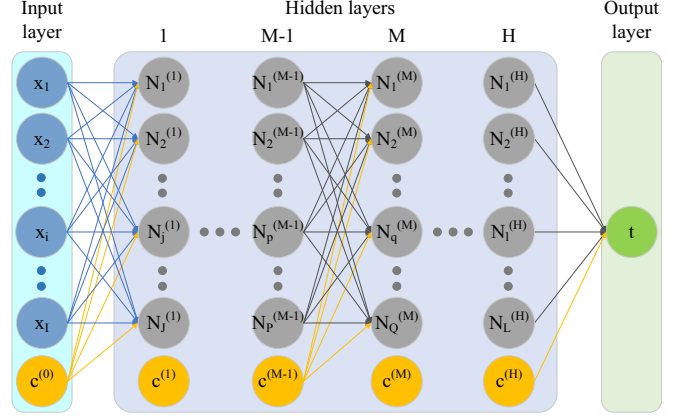


FIG. 1. The architecture of the deep Bayesian neural network (DBNN) utilized in this work. See the details in the text.

the hidden layers,

$$N_j^{(1)} = f\left(c_j^{(0)} + \sum_{i=1}^I d_{ji}^{(0)} x_i\right), \quad (1)$$

where  $N_j^{(1)}$  is the value transmitted to the  $j$ th neuron,  $d_{ji}^{(0)}$  is the weight factor between the  $i$ th feature and the  $j$ th neuron, and  $c_j^{(0)}$  is the bias for the  $j$ th neuron. The summation runs over all  $I$  features in the input layer. The hyperbolic tangent ( $\tanh$ ), having been successfully applied to the previous learning tasks within the Bayesian framework [25,33–38], is adopted for the nonlinear activation function  $f$ . Between two adjacent hidden layers, the values acquired by neurons are also transmitted using the feed-forward neural network with the  $\tanh$  activation function,

$$N_p^{(M-1)} = f\left(c_p^{(M-2)} + \sum_{o=1}^O d_{po}^{(M-2)} N_o^{(M-2)}\right), \quad (2)$$

$$N_q^{(M)} = f\left(c_q^{(M-1)} + \sum_{p=1}^P d_{qp}^{(M-1)} N_p^{(M-1)}\right). \quad (3)$$

In the above equations, the superscripts  $(M - 2)$ ,  $(M - 1)$ , and  $(M)$  denote the  $(M - 2)$ th,  $(M - 1)$ th, and  $(M)$ th hidden layers, whereas the subscripts  $o$ ,  $p$ , and  $q$  denote the  $o$ th,  $p$ th, and  $q$ th neurons in the  $(M - 2)$ th,  $(M - 1)$ th, and  $(M)$ th layers.  $O$ ,  $P$ , and  $Q$  are the numbers of neurons in the  $(M - 2)$ th,  $(M - 1)$ th, and  $(M)$ th layers, respectively. Finally, the  $t$  value is calculated from the last hidden layer with  $L$  neurons via

$$t = c^{(H)} + \sum_{l=1}^L d_l^{(H)} N_l^{(H)}. \quad (4)$$

### B. Input feature representations and target observable

To ensure the predictive accuracy for  $R_{\text{ch}}$ , searching for appropriate input feature representations and target observable is crucial in constructing the DBNN. Based on the previous  $R_{\text{ch}}$  studies using various conventional machine learning approaches [17–20], we design four types of input as candidates: (i)  $\mathbf{X} = \{A, Z, \delta\}$ .  $Z$  and  $A$  characterize the charge and

mass features of a given nucleus.  $\delta = 1, -1, 0$  for even-even, odd-odd, and odd-even nuclei, respectively, characterize the feature related to the pairing effect. (ii)  $X = \{A, Z, \delta, P\}$ .  $P = v_p v_n / (v_p + v_n)$  is the Casten factor related to the shell effect, where  $v_p$  and  $v_n$  are the effective numbers of valence protons and neutrons or proton and neutron holes with respect to the corresponding magic shells,  $Z = 2, 8, 20, 28, 50, 82, 126$  and  $N = 2, 8, 20, 28, 50, 82, 126, 184$  [39], respectively. This input is directly inherited from the approach of Dong *et al.* [18], using which the best predictive accuracy has been achieved to date. (iii)  $X = \{A, Z, \delta, v_p, v_n\}$ . In contrast to that of Dong *et al.* [18] where the Casten factor  $P$  was used as one feature representation,  $v_p$  and  $v_n$  are treated as two feature representations to consider the shell effect in the proton and neutron shells separately. (iv)  $X = \{A, Z, \delta, v_p, v_n, \beta_2\}$ .  $\beta_2$  is the quadrupole deformation factor for considering the nuclear deformation effect, and the  $\beta_2$  values calculated using the Weizsäcker-Skyrme mass model [40] are adopted in this work due to the lack of systematic data. Such application of a physical-informed feature in the input is a conventional technique to improve the predictive accuracy in machine learning. For example, in the previous study of  $\beta$ -decay half-lives using machine learning [34], Niu *et al.* incorporated the  $\beta$ -decay energies calculated with the Weizsäcker-Skyrme mass model [40] in the input. Recent work of Li *et al.* also showed the importance of physical-informed features in the prediction of heavy-ion fusion cross sections using the Light Gradient Boosting Machine [41].

One may notice that the complexity of the designed input increases, and this trend is consistent with the growing understanding of  $R_{\text{ch}}$  over time that the  $R_{\text{ch}}$  values depend significantly on nuclear mass, charge, pairing effect, shell effect, and deformation effect [42]. Keeping the four inputs in mind, we are going to discuss the input selection among them later.

Regarding  $t$  for the  $R_{\text{ch}}$  prediction,  $t$  for a given nucleus is defined as the residual between the corresponding rms charge radii from experiment and ‘‘theory,’’  $R_{\text{ch}}^{\text{exp}}$  and  $R_{\text{ch}}^{\text{th}}$ , following a conventional refinement strategy [17–19],

$$t \equiv R_{\text{ch}}^{\text{exp}} - R_{\text{ch}}^{\text{th}}, \quad (5)$$

where  $R_{\text{ch}}^{\text{th}}$  can be evaluated using either theoretical models or phenomenological formulas. Because it was demonstrated in Refs. [17,18] that the final predictive accuracy of various machine learning approaches depends weakly on the selection of initial models or phenomenological formulas for  $R_{\text{ch}}^{\text{th}}$ , we adopt a simple isospin-dependent parametrization [43] for  $R_{\text{ch}}^{\text{th}}$  in this work,

$$R_{\text{ch}}^{\text{th}} = a \times A^{1/3} \left[ 1 - b \times \frac{A - 2Z}{A} + \frac{c}{A} \right], \quad (6)$$

where  $a = 0.9584$  fm,  $b = 0.1590$ , and  $c = 2.1124$  are obtained from the best fit to all 1030 available experimental  $R_{\text{ch}}$  data for  $A \geq 12$  and  $Z \geq 6$  nuclei until now [11,12,44,45]. See the distribution of these nuclei in the nuclear chart of Fig. 2.

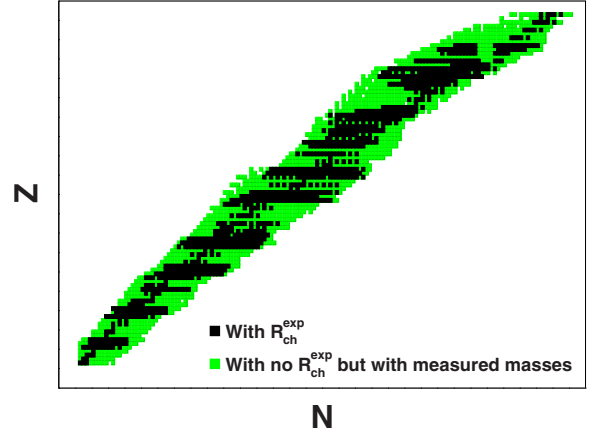


FIG. 2. Nuclear chart displaying the nuclei involved in this article. The black squares represent the 1030  $A \geq 12$  and  $Z \geq 6$  nuclei with available experimental  $R_{\text{ch}}$  values [11,12,44,45], whereas the green squares represent those with no experimental  $R_{\text{ch}}$  values but with experimental mass values [49,50].

### C. Training

The training of the DBNN is a process of optimizing the ‘‘model parameters,’’  $\omega = \{d^{(h)}, c^{(h)}\}$  ( $h = 0, 1, \dots, H$ ), using the Bayesian algorithm. In Bayesian formalism, the model parameters  $\omega$  in the DBNN are promoted to random variables, and the distribution of  $\omega$  is referred to as the prior distribution  $p(\omega)$ . After observing a set of training data  $\mathbf{D} = \{(X_1, t_1), (X_2, t_2), \dots, (X_i, t_i), \dots\}$ , the prior distribution is updated to the posterior distribution  $p(\omega|\mathbf{D})$ ,

$$p(\omega|\mathbf{D}) = \frac{p(\mathbf{D}|\omega)}{p(\mathbf{D})} p(\omega), \quad (7)$$

where  $p(\mathbf{D}|\omega)$  is a likelihood function and gives the probability of the observed data as function of the undetermined  $\omega$ , and  $p(\mathbf{D})$  is a normalization constant.  $p(\omega)$  is set to be the  $\Gamma$  distribution here. Following the standard practice, the likelihood function in Eq. (7) is set to be a Gaussian distribution such that  $p(\mathbf{D}|\omega) = \exp(-\chi^2/2)$  [33], where  $\chi^2$  is given by

$$\chi^2 = \sum_{i=1} \left[ \frac{t_i - F(X_i, \omega)}{\delta t_i} \right]^2. \quad (8)$$

In the equation,  $\delta t_i$  denotes the noise variance of the  $i$ th target observable. To introduce a source of randomness to reduce model-dependent effects [17,25,33],  $1/\delta t_i^2$  is taken to be a  $\Gamma$  prior distribution with unit parameter for easier calculations in mathematics allowing for the  $\Gamma$  distribution having been set as the conjugate prior distribution. During the DBNN training, one can optimize  $\omega$  by minimizing  $\chi^2$  in Eq. (8). In practice, however, rather than searching for the minimum value of  $\chi^2$ , the training is often terminated at any certain epoch when sufficient training is confirmed. Benefiting from the randomness sources introduced by  $p(\omega)$  and  $\delta t$ , the overfitting problem can be automatically avoided in the DBNN training process, permitting one to take the epoch number as large as possible in principle. After balancing the training performance and the computational time, the epoch number is set to be 100 000 in

this work. Note that this epoch number is already orders of magnitude larger than that used in the previous work [46].

After the DBNN is trained, one can make prediction for the  $t$  central value ( $\langle t \rangle$ ) for any nucleus by averaging the trained neural network over the posterior probability density of optimized  $\omega$ ,

$$\langle t \rangle = \int F(X, \omega) p(\omega | \mathbf{D}) d\omega. \quad (9)$$

For simplification, the high-dimensional integral in Eq. (9) is approximated via a Monte Carlo integration in which  $p(\omega | \mathbf{D})$  is sampled using the hybrid Markov chain Monte Carlo method [28]. The predicted value of nuclear rms charge radius  $R_{\text{ch}}^{\text{pred}}$  can be then calculated by adding  $\langle t \rangle$  from Eq. (9) and  $R_{\text{ch}}^{\text{th}}$  from Eq. (6). The error of  $R_{\text{ch}}^{\text{pred}}$  for the given nucleus  $\Delta R_{\text{ch}}^{\text{pred}}$  is quantified as  $\Delta R_{\text{ch}}^{\text{pred}} = \sqrt{\langle t^2 \rangle - \langle t \rangle^2}$ , where the  $\langle t^2 \rangle$  can be deduced via replacing  $F(X, \omega)$  with  $F^2(X, \omega)$  in Eq. (9).

### III. RESULTS AND DISCUSSION

#### A. Accuracy assurance

Besides the epoch number for the training, already discussed, there are also several hyperparameters in the DBNN that are important to the  $R_{\text{ch}}$  prediction and require manual tuning. To ensure the predictive accuracy of the DBNN, we here discuss the selection of the key hyperparameters related to the architecture, i.e., the number of hidden layers and the number of neurons in each layer, as well as the input feature representations mentioned above. Concerning the architecture design, three types of DBNN with 8-8 (denoting two hidden layers and eight neurons in each hidden layer, and similarly hereinafter), 16-16, and 8-8-8 architectures are studied as candidates. It should be emphasized that the DBNNs with higher complexity are not considered here, due to the fact that, given the limited amount of the  $R_{\text{ch}}$  data for training the DBNNs, statistical parsimony is a major consideration to enhance robustness [47]. Hence, considering the three architectures with the four inputs, there are twelve different DBNNs in total for selection.

A multiple training and validation approach is used to search for the DBNN with the most appropriate combination of architecture and input. For a DBNN with the given numbers of hidden layers and neurons in each layer and the given input, 90% of the 1030  $R_{\text{ch}}^{\text{exp}}$  values for  $A \geq 12$  and  $Z \geq 6$  nuclei [11,12,44,45] are sampled as training data, and the remaining 10% are used as validation data. This Monte Carlo sampling procedure is repeated for 200 times. Using the 200 sampled training data sets, the given DBNN is trained for 200 times independently. The 200 trained DBNNs are then applied to the nuclei in the corresponding validation data sets to calculate the respective  $R_{\text{ch}}^{\text{pred}}$  values. For each training and validation trial, since the validation data set is independent of the training data set, the accuracy for reproducing the  $R_{\text{ch}}^{\text{exp}}$  in the validation data set can provide an unbiased evaluation of the model “fit” with the corresponding training data set. We assess the predictive accuracy with the rms deviation  $\sigma_V$  between the  $R_{\text{ch}}^{\text{pred}}$  and  $R_{\text{ch}}^{\text{exp}}$

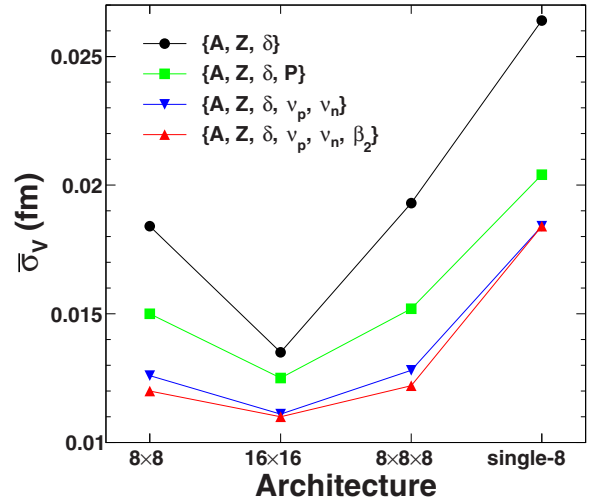


FIG. 3. Average predictive accuracy  $\bar{\sigma}_V$  versus DBNN architecture. Different symbols represent the results from the DBNNs with different types of input.

values following Refs. [17–20] as

$$\sigma_V = \sqrt{\frac{1}{N_V} \sum_{i=1}^{N_V} (R_{\text{ch},i}^{\text{pred}} - R_{\text{ch},i}^{\text{exp}})^2}, \quad (10)$$

where the subscript  $i$  represents the  $i$ th nucleus in the validation data set. The summation runs over all nuclei in the validation data set with total number  $N_V$ . Then, the average predictive accuracy  $\bar{\sigma}_V$  that reflects the average predictive performance of the given DBNN is calculated by averaging the  $\sigma_V$  values over all available 200 trials.

To visualize the dependence of  $\bar{\sigma}_V$  on the architecture and input selection, the obtained  $\bar{\sigma}_V$  values for the four inputs are plotted as a function of DBNN architecture in Fig. 3. As clearly observed in the figure, for all four inputs, the  $\bar{\sigma}_V$  minima commonly appear at the 16-16 architecture, and the  $\bar{\sigma}_V$  values at the 8-8 architecture are slightly smaller compared to those at the 8-8-8 architecture. In the recent work of Wang *et al.* [25], a similar result was also obtained: the predictive accuracy of the fission yields is the best for the double-layer neural work while adjusting the architecture of DBNNs from a single hidden layer to seven hidden layers. Both results indicate that to improve the predictive performance of DBNNs in tasks such as  $R_{\text{ch}}$  and fission yield predictions, increasing the neuron numbers in hidden layers is more effective than increasing the number of hidden layers, as the number of hidden layers reaches 2. This fact may be related to the limited number of training samples for both cases. Although the exact origin is unclear, the present observation of common  $\bar{\sigma}_V$  minima at the 16-16 architecture for all given inputs is enough to support the superiority of the 16-16 neural network in the task of  $R_{\text{ch}}$  prediction from a practical point of view. Moreover, one can observe that the  $\bar{\sigma}_V$  values show overall decrease as the complexity of input increases for all given architectures. This trend suggests the advantage of applying the six-feature input  $X = \{A, Z, \delta, v_p, v_n, \beta_2\}$  in the  $R_{\text{ch}}$  prediction. It can be

understood as more input information enabling the DBNN to acquire the correlation between the input and the raw data more precisely.

From the above analyses, the DBNN with the combination of 16-16 architecture and  $X = \{A, Z, \delta, \nu_p, \nu_n, \beta_2\}$ , having the minimum  $\bar{\sigma}_V$  value, proves to be optimal for predicting the existing  $R_{\text{ch}}^{\text{exp}}$  data, and will be adopted for the following studies. For completeness, we proceed to show the better predictive performance of the present DBNN compared to that from the previously used single-layer neural networks [17–20]. So far, the best predictive accuracy for  $R_{\text{ch}}$  has been achieved using a conventional Bayesian learning with eight neurons in a single layer (denoted as single-8) by Dong *et al.* [18]. Their and our approaches are both within the Bayesian framework, enabling us to make a direct comparison. For consistency, similar training and validation procedures are performed for the single-8 neural network of Dong *et al.* [18], and the obtained  $\bar{\sigma}_V$  values are shown at “single-8” in Fig. 3. One can find that regardless of the input difference, the application of the multilayer neural networks contributes to a significant decrease of  $\bar{\sigma}_V$  compared to the single-8 neural network, definitely demonstrating the superiority of the present DBNN approach.

### B. Generalization test

Since our primary goal is not just to memorize  $R_{\text{ch}}^{\text{exp}}$  using the present DBNN but to study the linear relationship of  $\Delta R_{\text{ch}}^{\text{mir}}$  and  $(N - Z)/A$  beyond the measured data with the aid of its extrapolating prediction, the generalization capability of the DBNN on the unmeasured data far from the  $\beta$ -stability line has to be carefully examined.

Due to the lack of experimental data far from the  $\beta$ -stability line, we here use a novel code for TDHF calculations based on Skyrme energy functionals (Sky3D)—which is able to solve the static or dynamic equations on a three-dimensional Cartesian mesh with isolated or periodic boundary conditions and no further symmetry assumptions, and has already had a wide variety of applications in nuclear structure, collective excitations, and nuclear reactions [29]—to generate the  $R_{\text{ch}}$  database. To avoid the model-dependent effect due to the accidental selection of a single Skyrme interaction parametrization, four effective interactions, SV-mas07, SV-mas08, SV-sym32, and SV-sym34 [48], are adopted in the present analyses. Using the four effective interactions, the  $R_{\text{ch}}$  values along all  $Z \geq 6$  isotope chains in the measured region [11,12,44,45] are calculated within the Sky3D framework. For a given isotope chain, the calculations run over all isotopes with available experimental masses [49,50]. See the distribution of the 2410 predicted  $R_{\text{ch}}$  in Fig. 2. For each nucleus, the  $R_{\text{ch}}$  value is then taken to be the average over the four effective interactions, and its error is taken to be the standard deviation. To distinguish from those of neural networks, the  $R_{\text{ch}}$  values from the Sky3D are referred to as  $R_{\text{ch}}^{\text{Sky3D}}$  here.

Of the 2410 obtained  $R_{\text{ch}}^{\text{Sky3D}}$  values, 1030 corresponding to the nuclei with the  $R_{\text{ch}}^{\text{exp}}$  data are taken to train the DBNN. To examine the generalization capability of the trained DBNN, extrapolating predictions are performed for the remaining 1380 nuclei with no experimental values, and the deduced

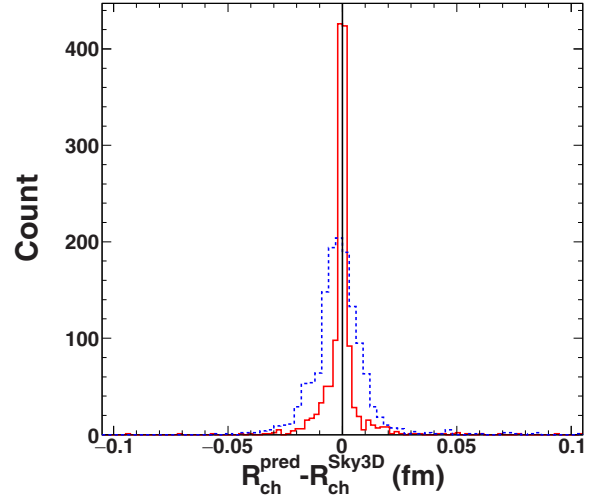


FIG. 4. Histograms of difference between  $R_{\text{ch}}^{\text{pred}}$  and  $R_{\text{ch}}^{\text{Sky3D}}$ ,  $R_{\text{ch}}^{\text{pred}} - R_{\text{ch}}^{\text{Sky3D}}$ , for the 1380 nuclei with no  $R_{\text{ch}}^{\text{exp}}$  values. The solid line is from the DBNN in this work, whereas the dashed line is from the single-8 neural network of Dong *et al.* [18]. The line at the origin is for guiding the eyes.

$R_{\text{ch}}^{\text{pred}}$  values are compared to those from the Sky3D calculations. The resulting histogram of the difference between the obtained central values of  $R_{\text{ch}}^{\text{pred}}$  and  $R_{\text{ch}}^{\text{Sky3D}}$  is shown by solid lines in Fig. 4. The line at the origin is for guiding the eyes. In the figure, the data points of  $R_{\text{ch}}^{\text{pred}}$  and  $R_{\text{ch}}^{\text{Sky3D}}$  difference form a sharp peak at the origin, reflecting a good one-to-one consistency between  $R_{\text{ch}}^{\text{pred}}$  and  $R_{\text{ch}}^{\text{Sky3D}}$ . Indeed, a further quantitative analysis gives a rather tiny rms deviation between the  $R_{\text{ch}}^{\text{pred}}$  and  $R_{\text{ch}}^{\text{Sky3D}}$  central values, 0.009 fm. These results are clear indication of the excellent generalization performance of the trained DBNN, and provide substantial support for the feasibility of utilizing the DBNN-predicted charge radii to investigate the linear  $\Delta R_{\text{ch}}^{\text{mir}}$  and  $(N - Z)/A$  relationship in the unmeasured region.

Similar to the analysis in Sec. III A, the generalization capability of the single-8 neural network is also examined to highlight the superiority of the present DBNN. Using the same training data set from Sky3D, the single-8 neural network of Dong *et al.* [18] is trained, and extrapolating predictions are made for the nuclei with no experimental  $R_{\text{ch}}$  using the trained neural network. The obtained histogram of the difference between  $R_{\text{ch}}^{\text{pred}}$  and  $R_{\text{ch}}^{\text{Sky3D}}$  is plotted by dashed line together with that of the DBNN in Fig. 4. As observed in the figure, the values of  $R_{\text{ch}}^{\text{pred}}$  and  $R_{\text{ch}}^{\text{Sky3D}}$  difference also assemble round the  $x = 0$  line, but with noticeably wider distributions compared to that of the DBNN. The rms deviation between the central values of  $R_{\text{ch}}^{\text{pred}}$  and  $R_{\text{ch}}^{\text{Sky3D}}$  is deduced to be 0.018 fm, twice the value obtained using the DBNN, demonstrating the better generalization capability of the present DBNN compared to that of previous single-layer neural networks.

### C. Mass-dependent linear relationship of $\Delta R_{\text{ch}}^{\text{mir}}$ and $(N - Z)/A$

In the above two subsections, we have shown that the DBNN with 16-16 architecture and  $X = \{A, Z, \delta, \nu_p, \nu_n, \beta_2\}$

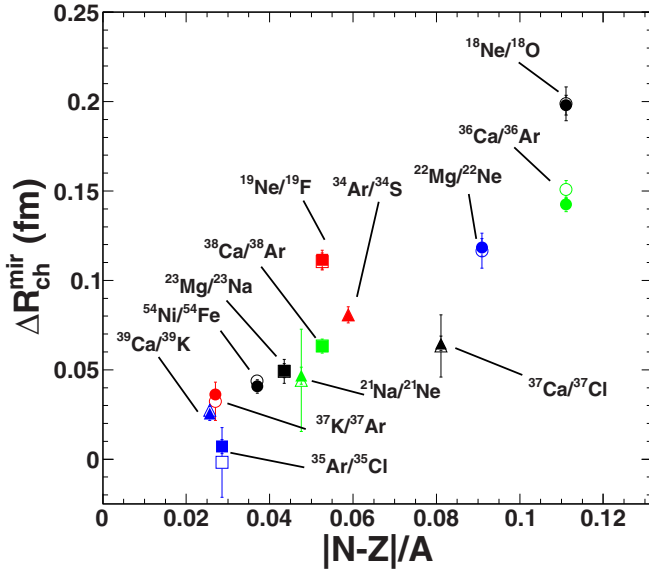


FIG. 5.  $\Delta R_{\text{ch}}^{\text{mir}}$  as a function of absolute isospin asymmetry  $|N - Z|/A$ . The results marked by filled symbols are the DBNN prediction, whereas those marked by open symbols are the experimental data [11,12,44,45].

cannot only well reproduce the existing data, but also has strong generalization capability to predict the unmeasured data far from the  $\beta$ -stability line. For practical study of the linear  $\Delta R_{\text{ch}}^{\text{mir}}$  and  $(N - Z)/A$  relationship in this work, the DBNN is retrained using the 1030 experimental data for  $A \geq 12$  and  $Z \geq 6$  nuclei [11,12,44,45]. Prior to the application, the practicability of the trained DBNN is carefully examined by comparing the  $\Delta R_{\text{ch}}^{\text{mir}}$  values deduced from the DBNN-predicted rms charge radii to all thirteen  $\Delta R_{\text{ch}}^{\text{mir}}$  values found among the 1030 data [11,12,44,45] as a function of absolute isospin asymmetry  $|N - Z|/A$  in Fig. 5. The results marked by filled and open symbols represent the predicted and measured data points, respectively. As found in the figure, the experimental  $\Delta R_{\text{ch}}^{\text{mir}}$  data appear only in the mass region of  $A \approx 20$ –60. An overall close agreement is achieved between the predicted and experimental  $\Delta R_{\text{ch}}^{\text{mir}}$  values, verifying the practicability of the present DBNN for studying the linear  $\Delta R_{\text{ch}}^{\text{mir}}$  and  $(N - Z)/A$  relationship.

Encouraged by the good performance in reproducing the existing  $\Delta R_{\text{ch}}^{\text{mir}}$  data, and the strong generalization capability having been proved in the above subsection, we extrapolate the  $R_{\text{ch}}$  for the unmeasured nuclei in the same  $A \approx 20$ –60 region where the experimental data are available using the DBNN trained by experimental  $R_{\text{ch}}$  data. For given elements, the extrapolating predictions are performed over all isotopes whose masses have been measured. The mirror pairs are searched among the predicted nuclei, and the  $\Delta R_{\text{ch}}^{\text{mir}}$  values are deduced using their  $R_{\text{ch}}^{\text{pred}}$  values. In Fig. 6(a), the deduced  $\Delta R_{\text{ch}}^{\text{mir}}$  values for all obtained mirror pairs are plotted as a function of  $|N - Z|/A$ , where the results with  $20 \leq A < 40$  and  $40 \leq A \leq 60$  are marked by filled circles and filled squares separately. Together with the DBNN-predicted results, the linear regression deduced from the coupled-cluster theory and

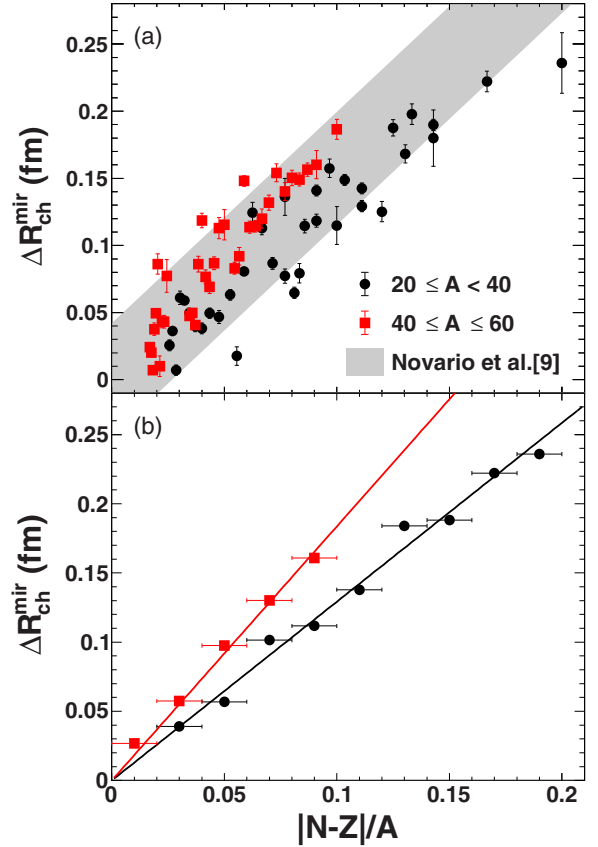


FIG. 6.  $\Delta R_{\text{ch}}^{\text{mir}}$  as a function of  $|N - Z|/A$ . (a) The results from the trained DBNN with 16-16 architecture and  $\mathbf{X} = \{A, Z, \delta, \nu_p, \nu_n, \beta_2\}$ , and those of  $20 \leq A < 40$  and  $40 \leq A \leq 60$  are shown by filled circles and filled squares, respectively. The shaded band is the linear regression with  $2\sigma$  confidence level which was deduced from the coupled-cluster theory and the auxiliary field diffusion Monte Carlo method by Novario *et al.* [9]. (b) Same as (a), but shown in different form. The lines are the fits to the data points with proportional functions. See the text for details.

the auxiliary field diffusion Monte Carlo method by Novario *et al.* [9],  $\Delta R_{\text{ch}}^{\text{mir}} = 1.574|N - Z|/A$  fm, is also plotted with  $2\sigma$  confidence level as a shaded band for comparison. One can observe from the figure that the  $\Delta R_{\text{ch}}^{\text{mir}}$  values of  $20 \leq A < 40$  and  $40 \leq A \leq 60$  both linearly increase with  $|N - Z|/A$ , and appear very consistent with the linear regression of Novario *et al.* [9] both in trend and in magnitude.

Most strikingly, two branches are observed in which the  $\Delta R_{\text{ch}}^{\text{mir}}$  values for  $40 \leq A \leq 60$  are systematically larger than those of  $20 \leq A < 40$ . This observation strongly indicates a significant mass dependence of the linear  $\Delta R_{\text{ch}}^{\text{mir}}$  versus  $|N - Z|/A$  relationship which has not been discovered in any previous experimental analysis related to  $\Delta R_{\text{ch}}^{\text{mir}}$ . For visual simplicity, an elegant replacement of the two-dimensional Fig. 6(a) is made by in turn averaging the obtained  $\Delta R_{\text{ch}}^{\text{mir}}$  values in ten bins from  $|N - Z|/A = 0$  to 0.2. The results are given in Fig. 6(b), where the errors along the  $x$  axis indicate the  $|N - Z|/A$  bin widths. The mass-dependent linear relationship of  $\Delta R_{\text{ch}}^{\text{mir}}$  and  $|N - Z|/A$  becomes more clear as shown in the figure. Fitting the  $\Delta R_{\text{ch}}^{\text{mir}}$  versus  $|N - Z|/A$  plots

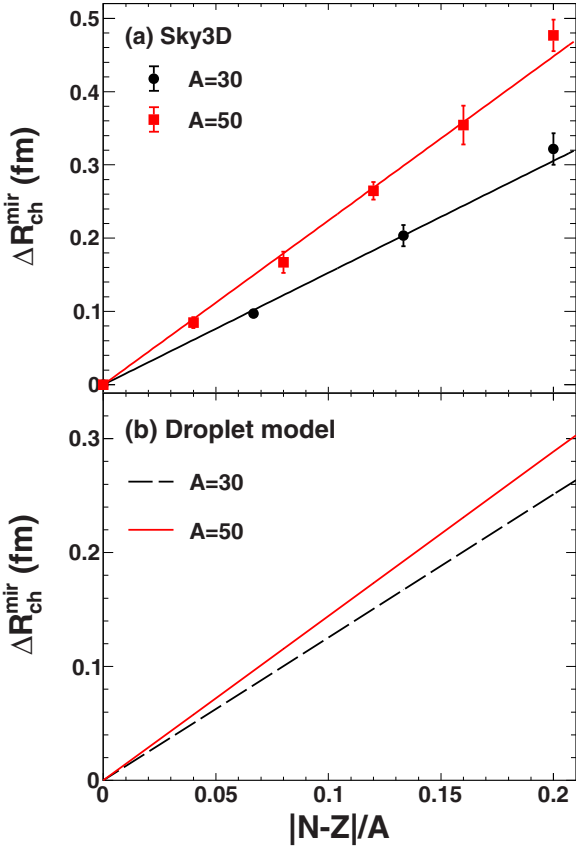


FIG. 7.  $\Delta R_{\text{ch}}^{\text{mir}}$  as a function of  $|N - Z|/A$ . (a) The average results from the Sky3D calculations [29] with the fixed masses  $A = 30$  and 50 but with different isospin asymmetries over four Skyrme effective interaction parametrizations, SV-mas07, SV-mas08, SV-sym32, and SV-sym34 [48]. The lines are the fits with proportional functions. (b) Same as (a), but from the droplet model with parameters adjusted by fitting the nuclear ground state masses and fission barriers [51].

for  $20 \leq A < 40$  and  $40 \leq A \leq 60$  of Fig. 6(b) using two proportional functions with the least-squares method, a slope for  $40 \leq A \leq 60$  is deduced to be 1.84, larger than that of  $20 \leq A < 40$ , 1.29, showing a significant mass dependence of the linear  $\Delta R_{\text{ch}}^{\text{mir}}$  versus  $|N - Z|/A$  relationship.

To investigate whether the mass-dependent linear behavior of  $\Delta R_{\text{ch}}^{\text{mir}}$  versus  $(N - Z)/A$  exists in nature, the microscopic Sky3D approach [29] and the macroscopic droplet model of Myers and Swiatecki [30] are used. For the Sky3D calculations, four Skyrme effective interaction parametrizations, SV-mas07, SV-mas08, SV-sym32, and SV-sym34 [48] are adopted to minimize the model-dependent effect, similarly to the analysis in Sec. III B. For the droplet model, the parameters adjusted by fitting the nuclear ground state masses and fission barriers [51] are adopted. Using both models, the  $\Delta R_{\text{ch}}^{\text{mir}}$  values are deduced for the mirror pairs with the fixed masses  $A = 30$  and 50 but with different isospin asymmetries. The resulting  $\Delta R_{\text{ch}}^{\text{mir}}$  versus  $|N - Z|/A$  relations are shown in Figs. 7(a) and 7(b), respectively, where those in Fig. 7(a) are the average results over the four Skyrme effective interactions. In the figure,  $\Delta R_{\text{ch}}^{\text{mir}}$  and  $|N - Z|/A$  predicted by the microscopic and macroscopic models both show

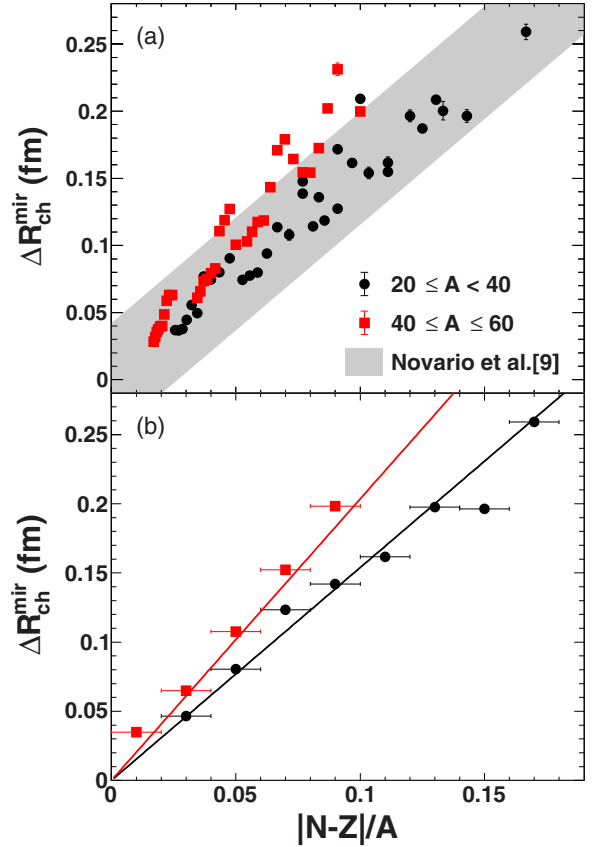


FIG. 8. Same as Fig. 6, but deduced from the trained DBNN with the  $R_{\text{ch}}^{\text{Sky3D}}$  data set obtained in Sec. III B.

significant mass-dependent linear relationships similar to the case of DBNN prediction. Such consistency strongly supports the physical existence of the mass dependence of the  $\Delta R_{\text{ch}}^{\text{mir}}$  versus  $(N - Z)/A$  linear relationship in nature. Additionally, comparing to the results from the trained DBNN with experimental data, Fig. 8, similar to Fig. 6 but deduced from the trained DBNN with the  $R_{\text{ch}}^{\text{Sky3D}}$  data set obtained in Sec. III B, is also plotted. Despite a minor difference in slope, the Sky3D results show a consistent mass-dependent behavior of the linear  $\Delta R_{\text{ch}}^{\text{mir}}$  and  $(N - Z)/A$  relationship with that of the DBNN shown in Fig. 6, confirming the physical existence of mass-dependent behavior.

#### D. Investigation of the origin of mass-dependent $\Delta R_{\text{ch}}^{\text{mir}}$ versus $(N - Z)/A$ linear relationship

With the indication of the existence of the mass-dependent  $\Delta R_{\text{ch}}^{\text{mir}}$  versus  $(N - Z)/A$  linear relationship in nature from both microscopic and macroscopic calculations, we proceed to pursue its origin in this subsection. For this purpose, we focus on the droplet model of Myers and Swiatecki [30], taking advantage of its simplicity in theory that permits one to provide a clear understanding of the physical picture. To facilitate understanding, it is worth showing the formalism of the droplet model. In the droplet model, the rms charge radius

for a spherical nucleus  ${}^A_Z X_N$  is written as

$$R_{\text{ch}}({}^A_Z X_N) = \sqrt{\frac{3}{5}} \left[ r_0(1 + \bar{\epsilon})A^{1/3} - \frac{N}{A}\tau + \frac{1.44}{35} \left( \frac{9}{2K_0} + \frac{1}{4a_{\text{sym}}^V} \right) Z^2 \right]. \quad (11)$$

In the equation,  $\bar{\epsilon}$  is a measure of the average deviation of the bulk density from the nuclear matter value. It mainly depends on nuclear mass, charge, and isospin asymmetry such that [30]

$$\bar{\epsilon} = (-2aA^{-1/3} + L\bar{\delta}^2 + cZ^2A^{-4/3})/K_0, \quad (12)$$

where

$$\bar{\delta} = \left[ \frac{N-Z}{A} + \frac{3c}{16Q}ZA^{-2/3} \right] / \left[ 1 + \frac{9a_{\text{sym}}^V}{4Q}A^{-1/3} \right]. \quad (13)$$

$\tau$  ( ${}^A_Z X_N$ ) in Eq. (11) is the neutron skin thickness, and has been deduced by Myers and Swiatecki as [30]

$$\tau({}^A_Z X_N) = \frac{3r_0}{2} \frac{a_{\text{sym}}^V \frac{N-Z}{A} - \frac{c}{12Q}ZA^{-1/3}}{1 + \frac{9a_{\text{sym}}^V}{4Q}A^{-1/3}}. \quad (14)$$

Concerning other parameters in Eqs. (11)–(14),  $K_0$  is the compressibility coefficient.  $L$  is the density-symmetry coefficient.  $a_{\text{sym}}^V$  is the volume symmetry energy coefficient.  $Q$  is the effective surface stiffness coefficient, and is often treated as an auxiliary constant of the surface symmetry coefficient  $a_{\text{sym}}^S$ ,  $Q = 9a_{\text{sym}}^S/4$  [31,32].  $r_0$ ,  $a$ ,  $c$ , and  $e$  are the nuclear radius constant, the surface energy coefficient, the Coulomb energy coefficient, and the electronic charge, respectively. Using Eqs. (11)–(14), the difference between a given mirror pair  ${}^A_Z X_N$  and  ${}^A_N Y_Z$  ( $Z > N$ ),  $\Delta R_{\text{ch}}^{\text{mir}}$ , can be mathematically deduced as

$$\begin{aligned} \Delta R_{\text{ch}}^{\text{mir}} &= R_{\text{ch}}({}^A_Z X_N) - R_{\text{ch}}({}^A_N Y_Z) \\ &= \sqrt{\frac{3}{5}} \frac{2r_0}{3} \frac{a_{\text{sym}}^V}{a_{\text{sym}}^S} \left( \frac{Z-N}{A} \right) \\ &\quad + \sqrt{\frac{3}{5}} \frac{r_0 c A}{K_0} \frac{(Z-N)}{A} + \sqrt{\frac{3}{5}} \frac{e^2 A}{35} \left( \frac{9}{2K_0} + \frac{1}{4a_{\text{sym}}^V} \right) \\ &\quad \times \frac{(Z-N)}{A} \\ &\quad + \sqrt{\frac{3}{5}} \frac{r_0 L}{K_0} \frac{\frac{c}{6a_{\text{sym}}^S} (Z-N)A^{-1/3} + \left( \frac{c}{12a_{\text{sym}}^S} \right)^2 A}{\left( 1 + \frac{a_{\text{sym}}^V}{a_{\text{sym}}^S} A^{-1/3} \right)^2} \\ &\quad \times \frac{(Z-N)}{A}. \end{aligned} \quad (15)$$

It can be found from Eq. (15) that there are four terms contributing to  $\Delta R_{\text{ch}}^{\text{mir}}$ , and each term has a factor  $(Z-N)/A$ . Taking the default parameters [51],  $K_0 = 240$  MeV,  $L = 100$  MeV,  $a_{\text{sym}}^V = 36.8$  MeV,  $Q = 17.0$  MeV ( $a_{\text{sym}}^S = 4Q/9 = 7.6$  MeV),  $r_0 = 1.18$  fm,  $a = 20.7$  MeV,  $c = 0.73$  MeV, and  $e^2 = 1.44$  MeV, the same as those used to produce Fig. 7(b), we can assess the contributions from the four terms to  $\Delta R_{\text{ch}}^{\text{mir}}$ . One

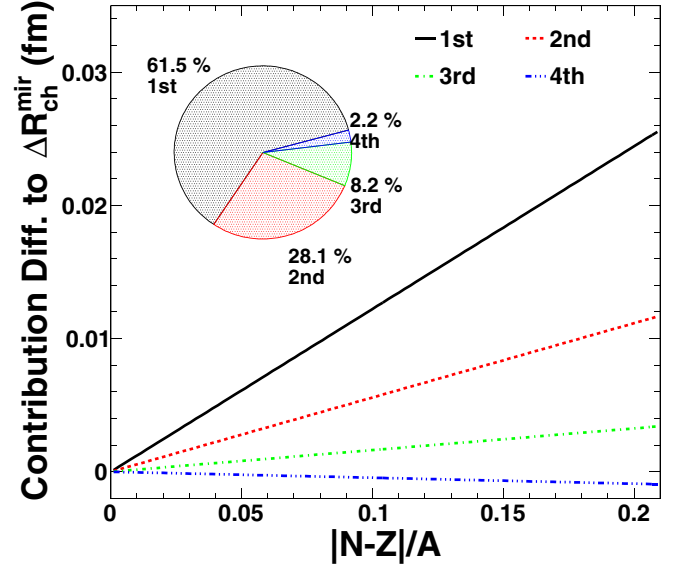


FIG. 9. Difference of the contributions to the mass-dependent  $\Delta R_{\text{ch}}^{\text{mir}}$  versus  $(N-Z)/A$  linear relationship for the  $A = 50$  and  $30$  mirror pairs. Difference lines are from different terms of Eq. (15). The absolute contribution magnitudes of the four terms to the mass-dependent behavior are deduced by integrating over the given interval in the figure. The inset pie chart shows the absolute fraction of the contributions from the four terms.

can easily understand that in the framework of the droplet model the overall linear trend of  $\Delta R_{\text{ch}}^{\text{mir}}$  versus  $(N-Z)/A$  is attributed to its  $(N-Z)/A$  proportionality as indicated by Eq. (15).

To further figure out the origin of the mass-dependent  $\Delta R_{\text{ch}}^{\text{mir}}$  versus  $(N-Z)/A$  linear relationship, we analyze the contributions of the four terms to the mass-dependent behavior within the droplet model. Taking the parameters as default, the values of the  $\Delta R_{\text{ch}}^{\text{mir}}$  contributions for the  $A = 30$  and  $50$  mirror pairs with different isospin asymmetries are calculated using Eq. (15). The relations of the obtained values from all four terms as a function of  $|N-Z|/A$  are further smoothed with proportional functions. Then, for the four terms, the differences between the obtained proportional relations of the  $A = 50$  and  $30$  mirror pairs are deduced and plotted in Fig. 9. The resultant lines in Fig. 9 convey abundant information about the mass-dependent behavior of  $\Delta R_{\text{ch}}^{\text{mir}}$  versus  $(N-Z)/A$ . That is, for a given term of Eq. (15), the absolute magnitude of the slope indicates the magnitude of the contribution to the  $\Delta R_{\text{ch}}^{\text{mir}}$  versus  $(N-Z)/A$  mass dependence, and the positive or negative sign of the slope indicates the enhancement or reduction effect on the mass dependence.

Combining Fig. 9 and the mathematical expression of Eq. (15), one can draw conclusions about the mechanism of the mass-dependent  $\Delta R_{\text{ch}}^{\text{mir}}$  versus  $(N-Z)/A$  linear relationship within the droplet model framework as follows.

- (1) The dominant effect on the mass-dependent relationship is an enhancement effect which originates from the  $A^{-1/3}$ -dependent denominator in the first term of Eq. (15). That is, the larger mass number the mirror



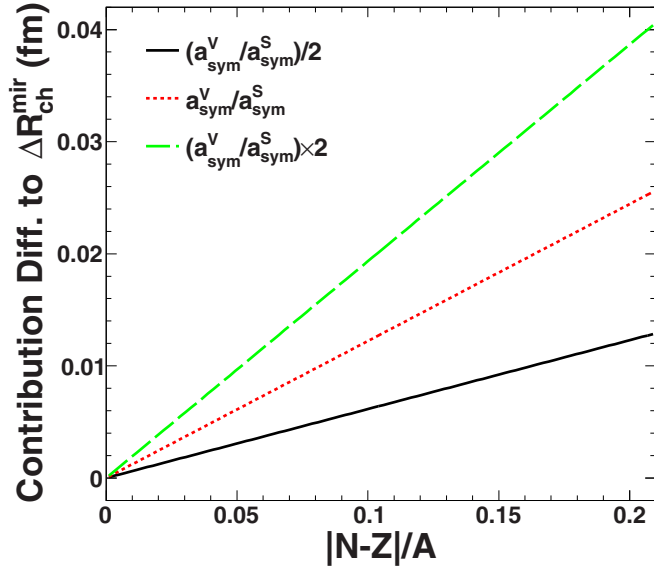


FIG. 10. Same as Fig. 9, but from the first term of Eq. (15) only. Different lines are corresponding to the different parametrizations for  $a_{\text{sym}}^V/a_{\text{sym}}^S$ .

pair has, the smaller the denominator will be, leading to the result that the mirror pairs with larger mass numbers have larger values of the first term. For the default parameter set of the droplet model, the absolute fraction of the first term contribution to the mass-dependent behavior is deduced to be 61.5% as given in the inset pie chart of Fig. 9.

- (2) The contributions to the mass dependence from the second and the third terms, 36.3% in total, are also positive. They are mainly related to the  $A$ -dependent bulk property difference of given mirror pairs.
- (3) The fourth term, with a minor contribution of around 2%, has a reduction effect on the mass dependence.

From these evaluations, one may notice that the significant contribution from the first term to the mass-dependent behavior of  $\Delta R_{\text{ch}}^{\text{mir}}$  versus  $(N - Z)/A$  is closely associated with the coefficient  $a_{\text{sym}}^V/a_{\text{sym}}^S$  in front of  $A^{-1/3}$ . Compared to the key parameters  $K_0$ ,  $L$ , and  $a_{\text{sym}}^V$  for describing the properties of nuclear matter,  $a_{\text{sym}}^S$  still has a rather large uncertainty, with values from 7.1 to 50.1 MeV [52–54] being found in the literature. The close correlation between  $a_{\text{sym}}^V/a_{\text{sym}}^S$  and the mass-dependent  $\Delta R_{\text{ch}}^{\text{mir}}$  versus  $(N - Z)/A$  linear relationship may open up a possibility to constrain the  $a_{\text{sym}}^S$  value in a narrower range. Fixing  $a_{\text{sym}}^V$ , we manually adjust the default coefficient  $a_{\text{sym}}^V/a_{\text{sym}}^S$  by dividing or multiplying it by a factor of 2, and recalculate the differences in contributions from the first term. The results are plotted together with that obtained using the default  $a_{\text{sym}}^V/a_{\text{sym}}^S$  in Fig. 10. As expected, the contribution difference from the first term shows a significant degree of sensitivity to changes in  $a_{\text{sym}}^V/a_{\text{sym}}^S$ . At this moment, the effective constraint to  $a_{\text{sym}}^S$  remains rather challenging,

since the present analysis is limited to the framework of the classical macroscopic droplet model only. As a result, we leave the task of constraining the  $a_{\text{sym}}^S$  value to future studies using more advanced microscopic approaches such as density functional theory, *ab initio* methods, etc. [13–15], which incorporate the spin-orbit effect, pairing effect, and other relevant microscopic factors. However, we stress here that the mass-dependent  $\Delta R_{\text{ch}}^{\text{mir}}$  versus  $(N - Z)/A$  linear relationship could be a suitable probe for extracting valuable information about the surface component of nuclear symmetry energy. Expanding the analyses in such a manner may provide deeper insights into the surface component of nuclear symmetry energy in future.

#### IV. SUMMARY

In summary, utilizing a newly developed deep Bayesian neural network (DBNN) approach, we investigate the linear relationship between the difference in mirror pair rms charge radii  $\Delta R_{\text{ch}}^{\text{mir}}$  and isospin asymmetry  $(N - Z)/A$  in unmeasured nuclei. The DBNN approach with optimized architecture and input features turns out to have excellent predictive capability for both existing rms charge radii  $R_{\text{ch}}$  data and the unmeasured data far from the  $\beta$ -stability line. This investigation reveals a significant mass-dependent linear relationship of  $\Delta R_{\text{ch}}^{\text{mir}}$  versus  $|N - Z|/A$  which has not been experimentally observed previously, for the nuclei with  $20 \leq A < 40$  and  $40 \leq A \leq 60$ . The physical existence and origin of the obtained mass-dependent  $\Delta R_{\text{ch}}^{\text{mir}}$  versus  $(N - Z)/A$  linear relationship is investigated by comparing it with the theoretical predictions of the microscopic Sky3D model and the macroscopic droplet model. The results indicate that the mass-dependent linear relationship is physical, with the degree of mass dependence closely associated with the ratio of volume and surface symmetry energy coefficients. The  $R_{\text{ch}}$  exploration in unstable nuclei beyond the  $\beta$ -stability line may soon be possible using the SCRIT facility at the RIKEN radioactive isotope (RI) factory [55] or ELISE at the future NUSTAR facility at FAIR [56]. The perspective of attaining valuable information on the surface contribution to nuclear symmetry energy may become accessible using the mass-dependent linear relationship of  $\Delta R_{\text{ch}}^{\text{mir}}$  and  $(N - Z)/A$  as a probe in the near future.

#### ACKNOWLEDGMENTS

We thank C. W. Ma, P. Dan, and C. Y. Qiao from Henan Normal University, Xixiang for the fruitful discussion. We also appreciate the anonymous referee's valuable comments and suggestions on this work in the review process. The key figures are uploaded as Supplemental Material [57] of this article. This research was supported by National Natural Science Foundation of China (Grants No. 12275186, No. 11705242, No. 11947416, No. 11905120, No. 12175156, and No. 11805138). This research was also supported by Sichuan Science and Technology Program (Grant No. 2024NSFSC0420).

- [1] K. Kreim *et al.*, *Phys. Lett. B* **731**, 97 (2014).
- [2] L. Xie *et al.*, *Phys. Lett. B* **797**, 134805 (2019).
- [3] X. F. Yang *et al.*, *Phys. Rev. Lett.* **116**, 182502 (2016).
- [4] B. A. Marsh *et al.*, *Nat. Phys.* **14**, 1163 (2018).
- [5] A. J. Miller *et al.*, *Nat. Phys.* **15**, 432 (2019).
- [6] S. V. Pineda *et al.*, *Phys. Rev. Lett.* **127**, 182503 (2021).
- [7] B. A. Brown, *Phys. Rev. Lett.* **119**, 122502 (2017).
- [8] B. A. Brown *et al.*, *Phys. Rev. Res.* **2**, 022035(R) (2020).
- [9] S. J. Novario, D. Lonardonì, S. Gandolfi, and G. Hagen, *Phys. Rev. Lett.* **130**, 032501 (2023).
- [10] Y. N. Huang, Z. Z. Li, and Y. F. Niu, *Phys. Rev. C* **107**, 034319 (2023).
- [11] I. Angeli and K. P. Marinova, *At. Data Nucl. Data Tables* **99**, 69 (2013).
- [12] T. Li *et al.*, *At. Data Nucl. Data Tables* **140**, 101440 (2021).
- [13] R. P. de Groote *et al.*, *Nat. Phys.* **16**, 620 (2020).
- [14] Á. Koszorús *et al.*, *Nat. Phys.* **17**, 439 (2021).
- [15] R. F. Garcia Ruiz *et al.*, *Nat. Phys.* **12**, 594 (2016).
- [16] W. D. Myers and W. J. Swiatecki, *Ann. Phys. (NY)* **211**, 292 (1991).
- [17] R. Utama *et al.*, *J. Phys. G: Nucl. Part. Phys.* **43**, 114002 (2016).
- [18] X. X. Dong *et al.*, *Phys. Lett. B* **838**, 137726 (2023).
- [19] Y. Ma, C. Su, J. Liu, Z. Ren, C. Xu, and Y. Gao, *Phys. Rev. C* **101**, 014304 (2020).
- [20] D. Wu, C. L. Bai, H. Sagawa, and H. Q. Zhang, *Phys. Rev. C* **102**, 054323 (2020).
- [21] Y. LeCun *et al.*, *Nature (London)* **521**, 436 (2015).
- [22] L. G. Pang *et al.*, *Nat. Commun.* **9**, 210 (2018).
- [23] X. Zhang *et al.*, *Phys. Rev. C* **105**, 034611 (2022).
- [24] R. D. Lasserri, D. Regnier, J. P. Ebran, and A. Penon, *Phys. Rev. Lett.* **124**, 162502 (2020).
- [25] Z. A. Wang and J. C. Pei, *Phys. Rev. C* **104**, 064608 (2021).
- [26] N. N. Ma, T. L. Zhao, W. X. Wang, and H. F. Zhang, *Phys. Rev. C* **107**, 014310 (2023).
- [27] W. He *et al.*, *Sci. China Phys. Mech. Astron.* **66**, 282001 (2023).
- [28] R. Neal, *Bayesian Learning for Neural Networks* (Springer, New York, 1996).
- [29] B. Schuetrumpf, P.-G. Reinhard, P. D. Stevenson, A. S. Umar, and J. A. Maruhn, *Comput. Phys. Commun.* **229**, 211 (2018).
- [30] W. D. Myers and W. J. Swiatecki, *Nucl. Phys. A* **336**, 267 (1980).
- [31] P. Danielewicz and J. Lee, *Nucl. Phys. A* **818**, 36 (2009).
- [32] P. Danielewicz and J. Lee, *Nucl. Phys. A* **922**, 1 (2014).
- [33] Z. M. Niu and H. Z. Liang, *Phys. Lett. B* **778**, 48 (2018).
- [34] Z. M. Niu, H. Z. Liang, B. H. Sun, W. H. Long, and Y. F. Niu, *Phys. Rev. C* **99**, 064307 (2019).
- [35] Z. A. Wang, J. Pei, Y. Liu, and Y. Qiang, *Phys. Rev. Lett.* **123**, 122501 (2019).
- [36] D. Peng *et al.*, *J. Phys. G: Nucl. Part. Phys.* **49**, 085102 (2022).
- [37] C. W. Ma *et al.*, *Chin. Phys. C* **46**, 074104 (2022).
- [38] X. B. Wei *et al.*, *Nucl. Sci. Tech.* **33**, 155 (2022).
- [39] M. W. Kirson, *Nucl. Phys. A* **798**, 29 (2008).
- [40] N. Wang and T. Li, *Phys. Rev. C* **88**, 011301(R) (2013).
- [41] Z. Li *et al.*, *Phys. Rev. C* **109**, 024604 (2024).
- [42] A. Bohr *et al.*, *Phys. Today* **23**(9), 58 (1970).
- [43] B. Nerlo-Pomorska and K. Pomorski, *Z. Phys. A* **348**, 169 (1994).
- [44] T. Day Goodacre *et al.*, *Phys. Rev. Lett.* **126**, 032502 (2021).
- [45] S. Malbrunot-Ettenauer *et al.*, *Phys. Rev. Lett.* **128**, 022502 (2022).
- [46] X. Wang, L. Zhu, and J. Su, *Phys. Rev. C* **104**, 034317 (2021).
- [47] L. Neufcourt, Y. Cao, W. Nazarewicz, and F. Viens, *Phys. Rev. C* **98**, 034318 (2018).
- [48] P. Klüpfel, P. G. Reinhard, T. J. Burvenich, and J. A. Maruhn, *Phys. Rev. C* **79**, 034310 (2009).
- [49] W. J. Huang, M. Wang, F. G. Kondev, G. Audi, and S. Naimi, *Chin. Phys. C* **45**, 030002 (2021).
- [50] M. Wang, W. J. Huang, F. G. Kondev, G. Audi, and S. Naimi, *Chin. Phys. C* **45**, 030003 (2021).
- [51] W. D. Myers, *Droplet Model of Atomic Nuclei* (Plenum, New York, 1977).
- [52] W. D. Myers and W. J. Swiatecki, *Ann. Phys. (NY)* **55**, 395 (1969).
- [53] W. D. Myers and W. J. Swiatecki, *Phys. Rev. C* **62**, 044610 (2000).
- [54] K. Pomorski and J. Dudek, *Phys. Rev. C* **67**, 044316 (2003).
- [55] T. Ohnishi *et al.*, *Phys. Scr.* **T166**, 014071 (2015).
- [56] T. Suda and H. Simon, *Prog. Part. Nucl. Phys.* **96**, 1 (2017).
- [57] See Supplemental Material at <http://link.aps.org/supplemental/10.1103/PhysRevC.110.014316> for the key figures having been provided in the response letter during the anonymous review process.